

# Helimagnetic structure of $\text{YMn}_2$ observed by means of nuclear magnetic resonance and neutron diffraction

H Nakamura<sup>1,3</sup>, N Metoki<sup>2</sup>, S Suzuki<sup>1</sup>, F Takayanagi<sup>1,4</sup> and M Shiga<sup>1</sup>

<sup>1</sup> Department of Materials Science and Engineering, Kyoto University 606-8501, Japan

<sup>2</sup> Japan Atomic Energy Research Institute, Tokai, Ibaraki 319-1195, Japan

E-mail: nakamura@nmr.mtl.kyoto-u.ac.jp

Received 25 May 2000, in final form 11 October 2000

## Abstract

We approach the helimagnetic structure of the itinerant-electron magnet  $\text{YMn}_2$ , in which the Mn sublattice forms a geometrically frustrated corner-sharing tetrahedral lattice, by means of both low-energy neutron diffraction and precise nuclear magnetic resonance (NMR) experiments, by modifying the magnetic state by Tb substitution (the introduction of lattice inhomogeneity), and by considering the origin of the tetragonal lattice distortion detected below  $T_N$ . The spin reorientation induced by the Tb substitution from the helical state with the propagation vector  $\vec{Q} = [\tau 0 1]$  ( $\tau = 0.018$ ) and with spins lying in the  $\{100\}$  plane to that with  $\vec{Q} = [\tau \tau 1]$  ( $\tau = 0.015$ ) and  $\{111\}$ -plane rotation is interpreted as symmetry lowering from a coherent proper screw state with a high magnetic symmetry to an asymmetric but locally preferable configuration with the easy-plane anisotropy perpendicular to the local symmetry axis. Treating the magnetic state as a weakly coupled assembly of one-dimensional antiferromagnetic spin chains, which is realized as a result of the partial release of the frustration, and taking into consideration the lattice symmetry, the possibility of double-axial helical structures arises and is discussed. In this study, all the inconsistency among previously reported NMR spectra is removed, and the strong frequency dependence of the spin-echo decay time  $T_2$  found unexpectedly is explained in terms of a phenomenological model taking into consideration the dynamic motion of electron spins in the locally anisotropic magnetic system.

## 1. Introduction

Magnetic structure is usually determined by neutron diffraction experiments. In general, however, magnetic structures thus determined include some ambiguity, particularly as regards the directions of spins in highly symmetric lattices [1]. To distinguish between these apparently

<sup>3</sup> Author to whom any correspondence should be addressed.

<sup>4</sup> Present address: Advantest Laboratories Limited, 48-2 Matsubara, Kamiyashi, Aoba-ku, Sendai 989-3124, Japan.

degenerate structures, nuclear magnetic resonance (NMR) is often useful [2] because NMR, as a local probe, gives information in real space, which is complementary to that in reciprocal space obtained by diffraction methods. In the present study, we use both neutron diffraction and NMR in discussing the magnetic structure in a highly symmetric lattice.

The cubic Laves phase compound  $\text{YMn}_2$  exhibits helical magnetic ordering with an extremely long period below  $T_N \simeq 100$  K [3–5]. However, it seems that the precise magnetic structure, including the spin direction and the origin of the long-period modulation, have not been fully understood. It relates to the geometrical frustration of antiferromagnetic interaction on the corner-sharing tetrahedral lattice (see figure 1(a)) inherent to the cubic Laves phase structure, with lattice parameter  $a \simeq 7.7$  Å. It is well known that the nearest-neighbour antiferromagnetic interaction frustrates in a regular tetrahedron and that if the four spins satisfy

$$\vec{s}_1 + \vec{s}_2 + \vec{s}_3 + \vec{s}_4 = 0 \quad (1)$$

the total energy is always the lowest. The atomic positions  $\vec{r}_i$  of the spins  $\vec{s}_i$  are defined in section 4.1 and indicated in figure 1(a). Therefore, in the corner-sharing tetrahedral lattice, the magnetic ground state has a macroscopic number of degeneracies.

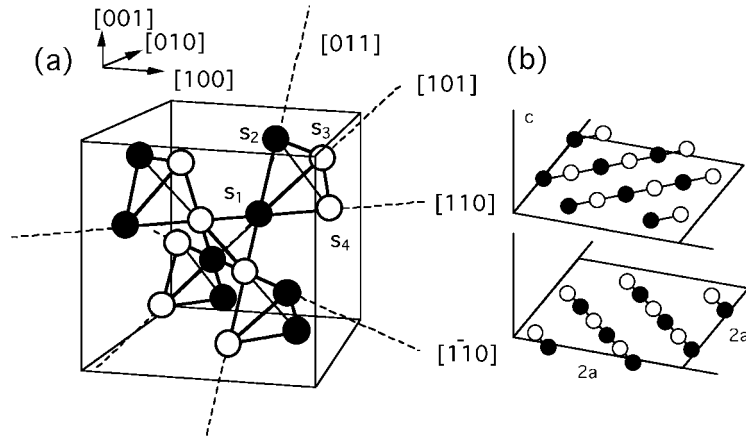


**Figure 1.** (a) The magnetic structure of  $\text{YMn}_2$  (NSK model) proposed by Nakamura, Shiga and Kawano [6] (●: up spins; ○: down spins). (b) Neighbouring  $c$ -planes, which are shown to emphasize the  $[110]$  and  $[1\bar{1}0]$  antiferromagnetic spin chains.

Extensive investigation of  $\text{YMn}_2$  started after the antiferromagnetic ordering was found by the first neutron diffraction measurement [6]. The transition is of first order, accompanied by a huge discontinuous volume change with  $\Delta V/V \simeq 5\%$  and a thermal hysteresis. On the basis of a neutron diffraction experiment using a neutron beam with a wavelength of  $\lambda = 1.0$  Å, Nakamura, Shiga and Kawano [6] proposed an antiferromagnetic structure with  $\vec{Q} = [001]$  (with an ordered moment of  $2.7 \mu_B/\text{Mn}$ ) as shown in figure 1(a) (this will be denoted as the NSK model), where  $\vec{Q}$  is the propagation vector of the face-centred cubic (fcc) sublattice (see section 4.1). This is known to be one of the most stable antiferromagnetic structures in this lattice [7]. In the NSK model, the magnitudes of the moments are the same, i.e.

$$s_1 = s_2 = s_3 = s_4. \quad (2)$$

This restriction was always applied in the literature cited hereafter and is also assumed in the present study. Subsequently, a small tetragonal distortion below  $T_N$  ( $1 - c/a \simeq 0.5\%$ ) was confirmed by high-resolution experiments [4].

Before discussing the spin direction, let us examine in more detail the black-and-white lattice shown in figure 1; we are considering only the Ising-type spin degree of freedom. Three one-dimensional  $\langle 110 \rangle$  spin chains cross at each spin site due to the geometrical characteristics. Let us inspect each (001) plane; one such is extracted in figure 1(b) to allow us to exaggerate its characteristics. In each (001) plane there are one-dimensional [110] (or  $[1\bar{1}0]$ ) chains, in which nearest-neighbour spins are coupled as  $+ - + -$ . That is, the nearest-neighbour antiferromagnetic coupling is operative in the  $c$ -planes. The chains belonging to neighbouring (001) planes are perpendicular to each other. The [110] and  $[1\bar{1}0]$  chains are equivalent not only crystallographically but also magnetically. On the other hand, if we follow the spin arrangement in the other chains, say along the [011] direction, the spins are coupled as  $+ + - -$ . That is, the NSK structure is tetragonal as regards magnetic symmetry. In addition, for two nearest-neighbour spins belonging to neighbouring chains in different  $c$ -planes, one is  $+$  and the other is  $-$ , implying that no magnetic interaction acts between the chains due to cancellation. In spite of the crystallographic equivalence of the  $\langle 110 \rangle$  chains, the magnetic interaction between the (001) planes is ‘decoupled’ to compensate for the tight antiferromagnetic coupling in the [110] and  $[1\bar{1}0]$  chains. In other words, the NSK structure is characterized as weakly coupled one-dimensional antiferromagnetic chains. This reduced dimensionality of the antiferromagnetic interaction is one of the consequences of the frustration.

Although, in figure 1(a), the [001] direction is specific with respect to the magnetic coupling, the [100], [010] and [001] directions should be degenerate under ideal cubic symmetry and, therefore, the dynamic state which is the linear combination of the three states would be the ground state. On the other hand, if the lattice symmetry is lowered, particularly to tetragonal, for any reason, the static NSK configuration is expected to be realized. Therefore the observed small tetragonal distortion seems to be consistent with the NSK model; the tetragonal  $c$ -axis coincides with the magnetic [001] axis [4]. The distortion with  $c < a$  is not inconsistent with the above-mentioned reduced magnetic dimensionality because, for manganese Laves phase compounds, generally, the larger the interatomic distance is, the more stable the magnetic moment is, and hence the stronger the antiferromagnetic interaction is. We may conclude that the magnetic ordering of YMn<sub>2</sub> is realized when the energy gain due to the partial release of the frustration overcomes the loss of elastic energy associated with the symmetry lowering in the crystal. In addition, this means that there is strong magneto-crystalline (magnetovolume) coupling in the YMn<sub>2</sub> system. However, this argument is valid only when considering the Ising-type spin degree of freedom. If we take into account the spin orientation and/or the helical modulation, the situation is more complicated and controversial.

When the NSK model was proposed, the spin axis was argued to be along the [111] direction by analysing intensities of magnetic Bragg peaks. At that time, a rhombohedral distortion was accordingly suggested [9], but was deemed to be refuted subsequently by high-resolution experiments [4], after some debate [9–11]. After the initial work, Ballou *et al* [3] performed again neutron diffraction experiments using a long-wavelength neutron beam ( $\lambda = 2.483 \text{ \AA}$ ) and found splittings of the magnetic Bragg peaks. They proposed a helical modulation of the antiferromagnetic structure ( $2.7 \mu_{\text{B}}/\text{Mn}$ ) with an extremely long period of about 400  $\text{\AA}$ . They determined the propagation vector  $\vec{Q} = [\tau 0 1]$  with  $\tau = 0.02$ . Within this model, the best fit to neutron diffraction intensities is obtained with Mn spins rotating in the  $a$ -plane (the (100) plane). Note that Ballou *et al* [8] also suggested the possibility of a multi-axial structure from consideration of the magnetic anisotropy in YMn<sub>2</sub>. Further, Cywinski *et al* [4] performed high-resolution powder neutron diffraction experiments using a pulsed neutron instrument and determined the modulation vector  $\vec{Q} = [\tau \tau' 1]$  with  $\tau = 0.018$  and  $\tau' = 0.003$ , i.e. the Mn spins rotating in the [100] direction with a period of 430  $\text{\AA}$  and in the [010] direction with a period of as much as 2500  $\text{\AA}$ . The best fit to the data was again obtained

with the Mn spins ( $2.8 \mu_B/\text{Mn}$ ) lying in the (100) plane. It seems that, with the Mn spins lying in the  $a$ -plane (the (100) plane) and rotating mainly along the  $a$ -axis (the [100] direction), it is somewhat difficult to explain the tetragonal distortion in the  $c$ -direction (the [001] direction) because we are not able to explain why the  $a$ -plane is selected as the spin-rotation plane from the crystallographically equivalent  $a$ - and  $b$ -planes. Taking this symmetry problem seriously, Vokhnyanin *et al* [5] proposed a different model with  $\vec{Q} = [1+\tau \ 0 \ 1+\tau]$  ( $\tau = 0.0077$ ) based on their neutron diffraction result ( $\lambda = 2.42 \text{ \AA}$ ). In their model, Mn spins ( $2.6 \mu_B/\text{Mn}$ ) lie in the (001) plane and some nearest-neighbour spins are mutually perpendicular in the plane. The magnetic structure is modulated along the [101] direction with a period of about  $700 \text{ \AA}$ . Thus, the spin direction of  $\text{YMn}_2$  is still controversial. This is related to the facts that the crystal symmetry of  $\text{YMn}_2$  is high and that the neutron diffraction method is not always infallible in determining the spin direction in a highly symmetric lattice.

Since the straightforward approach is thus limited, we access this problem from different viewpoints. We make the following points.

- (i) By applying perturbation, we speculate on the original state by inspecting the variation.
- (ii) To supplement the reciprocal-space information obtained by diffraction methods, we obtain real-space information by performing experiments with local probes.
- (iii) We apply physically reasonable restrictions to select models of the spin structure.

As regards (i), we recently performed high-resolution neutron diffraction measurements of  $\text{Y}_{0.97}\text{Tb}_{0.03}\text{Mn}_2$  (which will be denoted as  $\text{Y}(\text{Tb})\text{Mn}_2$ ) using a low-energy neutron source with  $\lambda = 4.750 \text{ \AA}$  and succeeded in detecting an appreciable change in the neutron diffraction pattern [16]. We selected Tb as the dopant because Tb has an atomic volume close to that of Y, and therefore does not affect the stability of the Mn moments. The Tb moments are so dilute that they behave paramagnetically down to about 1 K and do not interact appreciably with the Mn sublattice. The neutron diffraction profile of  $\text{Y}(\text{Tb})\text{Mn}_2$  was interpreted in terms of a helix with  $\vec{Q} = [\tau \ \tau \ 1]$  where  $\tau = 0.015$ . This indicates that the direction of the propagation vector changes from [100] to [110] on substituting only 3% Tb for Y. On the other hand, the crystal distortion was found to be tetragonal as in  $\text{YMn}_2$ .

As for (ii), further useful information on the magnetic structure is given by the NMR spectrum measured for the ordered state. Usually, the signal intensity at a certain frequency is considered to measure the population of the atoms which ‘feel’ the corresponding internal field. At an early stage, Yoshimura and Nakamura [12] reported an NMR spectrum with two peaks with an intensity ratio of 1:3, which was interpreted assuming the NSK model and anisotropy in the internal field. The spin direction was argued to be parallel to the [111] axis on the basis of the intensity ratio. However, this spectrum was revealed to be inconsistent with homogeneous spin rotation in the (100) plane, since such a helix leads to a doublet spectrum with the peaks having equal intensity (see section 4.2). After the discovery of the long-period modulation, Bertier *et al* [13] reported a different NMR spectrum, which has a single peak with a long tail on the high-frequency side. This spectrum was explained assuming an inhomogeneous modulation of the helix. Furthermore, an exactly intermediate spectrum was also reported by other authors [14, 15]. Thus, there have been appreciable differences in the experimental results, although earlier workers have treated them as the principal information for determining the spin direction. This situation has led to confusion in discussing the magnetic structure. Therefore it seems to be necessary to measure the NMR spectrum of  $\text{YMn}_2$  in more detail.

As regards (iii), we believe that the magnetic ordering of  $\text{YMn}_2$  is realized as a result of the partial release of the frustration as mentioned above. In addition, we respect the correspondence between magnetic and crystallographic symmetry in the present study.

The primary purpose of this study is to clarify the origin of the discrepancies among the previously reported NMR spectra of YMn<sub>2</sub> and to give balanced information to support discussion of the magnetic structure. The strong frequency dependence of the spin-echo decay time  $T_2$  found unexpectedly in this study is explained by a simple phenomenological model taking into consideration the dynamic motion of electron spins. The final aim is to discuss the more normal magnetic structure of YMn<sub>2</sub>. Here we treat the ordered state of YMn<sub>2</sub> as an assembly of weakly coupled one-dimensional antiferromagnetic spin chains. From comprehensive analyses of both NMR and neutron diffraction data, we argue for the possibility of a multi-axial helimagnetic structures.

A part of this study has already been published in conference proceedings [17, 18].

## 2. Experimental procedures

Polycrystalline samples of YMn<sub>2</sub> and Y<sub>0.97</sub>Tb<sub>0.03</sub>Mn<sub>2</sub> were prepared from 99.9% pure Y and Tb and 99.95% pure Mn in nominal concentrations by arc melting in an argon atmosphere. The ingots were annealed for a week in evacuated quartz tubes at 800 °C. No foreign phase other than of C15 type was detected for either of the samples by means of x-ray and neutron powder diffraction. To characterize the samples, the temperature dependence of the magnetic susceptibility was measured by a SQUID magnetometer (Quantum Design MPMS-2) under a field of 1 T. For nuclear resonance measurements the samples were crushed into fine powder with the particle diameter less than 50 μm to avoid the skin-depth effect. Spin-echo measurements were made with a home-made phase-coherent-type pulsed spectrometer. The spin–lattice relaxation time  $T_1$  was measured by the saturation–recovery method with the appropriate number of saturation comb pulses. The gyromagnetic ratio for <sup>55</sup>Mn,  $\gamma/2\pi = 10.50 \text{ MHz T}^{-1}$ , was used for the analyses. Since the Mn site (16d site) has trigonal symmetry, the <sup>55</sup>Mn nucleus with the nuclear spin  $I = \frac{5}{2}$  ‘feels’ an electric field gradient with the asymmetry parameter  $\eta = 0$ . Neutron diffraction measurements were carried out by using the High Resolution Powder Diffractometer (HRPD) and the Low-energy Triple Axis Spectrometer (LTAS) installed at the reactor JRR-3M in Japan Atomic Energy Research Institute (JAERI). The (311) plane of a Ge monocrystal was used as the monochromator for HRPD. The collimation was 6′–20′–6′. When using LTAS, three-axis measurements were performed to achieve the required resolution. The (002) plane of pyrolytic graphite was used for both monochromator and analyser. The collimation was 28′–40′–20′–40′. The wavelengths of the incident neutrons are 1.823 and 4.750 Å for HRPD and LTAS, respectively.

## 3. Experimental results

### 3.1. Magnetic susceptibility

Temperature dependences of the magnetic susceptibility measured for YMn<sub>2</sub> and Y(Tb)Mn<sub>2</sub> are shown in figure 2. The inverse susceptibility is also shown for Y(Tb)Mn<sub>2</sub>. Each of the samples exhibits a magnetic transition at around 100 K accompanied by a large thermal hysteresis. The result for YMn<sub>2</sub> is practically the same as those reported in the literature [19] although the low-temperature upturn is considerably suppressed for the present sample, indicating that the large upturn observed for previous samples is extrinsic. The susceptibility of Y(Tb)Mn<sub>2</sub> is two orders larger in magnitude than that of YMn<sub>2</sub> and shows a Curie–Weiss-like temperature dependence down to 5 K, which is ascribed to paramagnetic Tb moments; Tb moments are dilute enough not to interact with each other. The substitution of a small amount of Tb does not affect the transition temperature, indicating that the magnetism of the

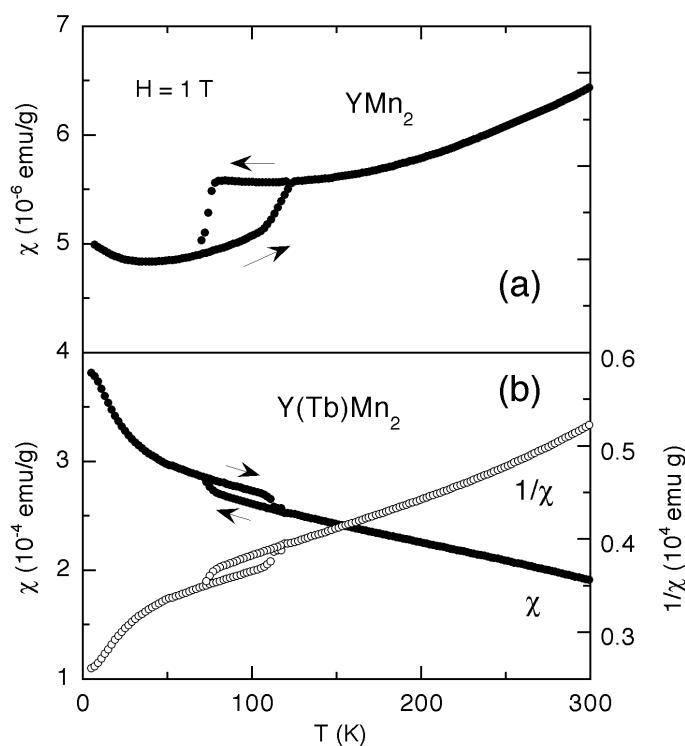


**Figure 2.** The temperature dependence of the magnetic susceptibility ( $\bullet$ ) for  $\text{YMn}_2$  (a) and  $\text{Y}_{0.97}\text{Tb}_{0.03}\text{Mn}_2$  (b). The inverse susceptibility ( $\circ$ ) is also shown for  $\text{Y(Tb)Mn}_2$ .

Mn sublattice is scarcely modified on a macroscopic scale. In contrast to the case for  $\text{YMn}_2$ , however, the susceptibility increases slightly below  $T_N$ , suggesting that the effective magnetic interaction between Tb moments is modified by the magnetic ordering of the Mn sublattice; the magnitude of the Weiss temperature decreases below  $T_N$ .

### 3.2. Paramagnetic properties: the Knight shift

To obtain information on the hyperfine coupling, particularly its anisotropy, we measured the temperature dependence of the paramagnetic  $^{55}\text{Mn}$  NMR spectrum for  $\text{YMn}_2$ . An example of a field-swept spectrum measured at 100 K is shown in figure 3, which shows well-resolved quadrupolar splittings for  $I = \frac{5}{2}$  with  $\eta = 0$ . The nuclear quadrupole frequency  $\nu_Q$  (the magnitude of the electric field gradient), estimated from the separation of the first-order satellites, is shown in figure 4 as a function of temperature. With increasing temperature,  $\nu_Q$  decreases monotonically; this is mainly ascribable to the thermal expansion. An enlargement of the centre line (transitions of  $m = +\frac{1}{2} \leftrightarrow -\frac{1}{2}$ ), shown in the inset of figure 3, exhibits an asymmetric shape due mainly to the second-order quadrupolar effect. However, assuming isotropy of the Knight shift, we failed to explain the shape—in particular, the separation of two peaks—indicating that the anisotropy should be taken into account. To estimate the Knight-shift parameters  $K_{\parallel}$  and  $K_{\perp}$ , which are the components parallel and perpendicular to the quantization axis, we compared the experimental results with computer-generated powder patterns. Here we assumed coincidence of the principal axis of the Knight-shift tensor with the local symmetry axis  $\langle 111 \rangle$  and used the values of  $\nu_Q$  estimated above. The broken and

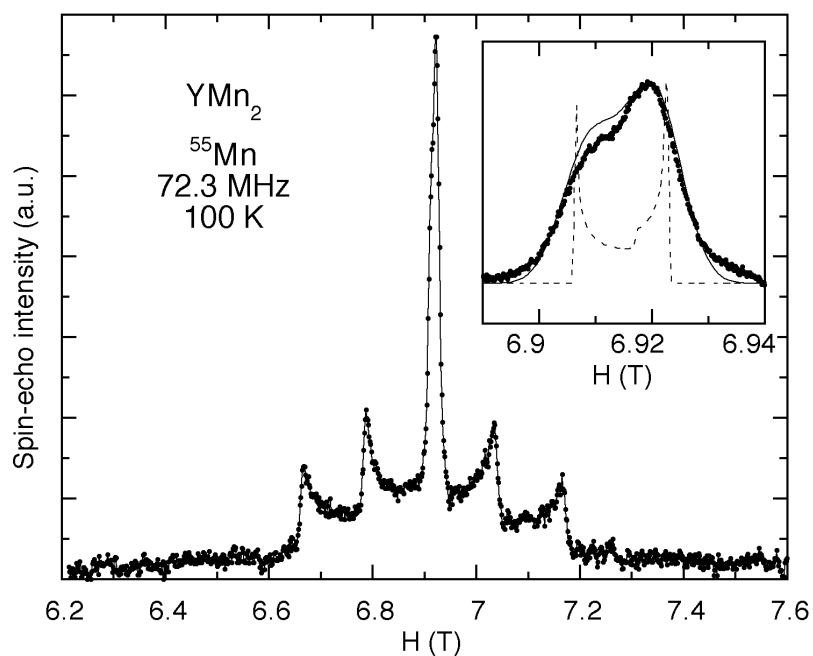


**Figure 3.** The paramagnetic  $^{55}\text{Mn}$  NMR spectrum of  $\text{YMn}_2$  measured at 72.3 MHz and 100 K. The inset shows an enlargement of the centre line (---: the calculated pattern with appropriate Knight-shift and quadrupolar parameters; —: its Gaussian-convoluted pattern).

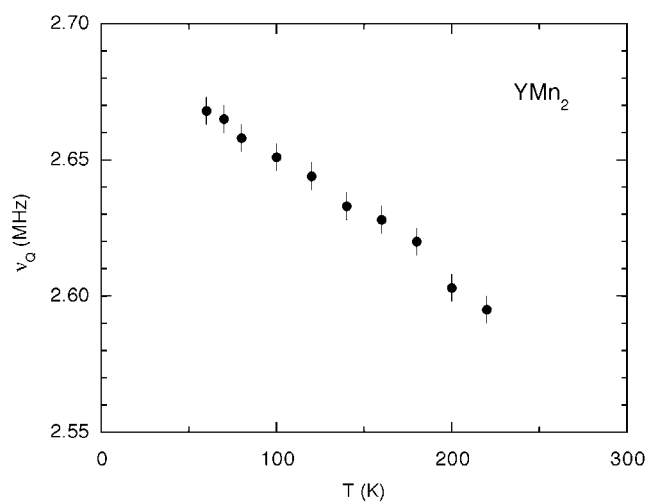


**Figure 4.** The temperature dependence of the pure quadrupole frequency  $\nu_Q$  for  $\text{YMn}_2$ , which was estimated from the splitting of the first-order satellites in the paramagnetic spectrum (measured in the temperature-decreasing process).

solid curves in the inset are the results calculated without and with consideration of the Gaussian-type inhomogeneous linewidth, respectively. The temperature dependences of  $K_{\parallel}$  and  $K_{\perp}$  thus obtained for the paramagnetic phase are shown in figure 5(a). It is notable that  $K_{\parallel}$  and  $K_{\perp}$  are proportional to the bulk susceptibility (figure 2(a)), with negative hyperfine

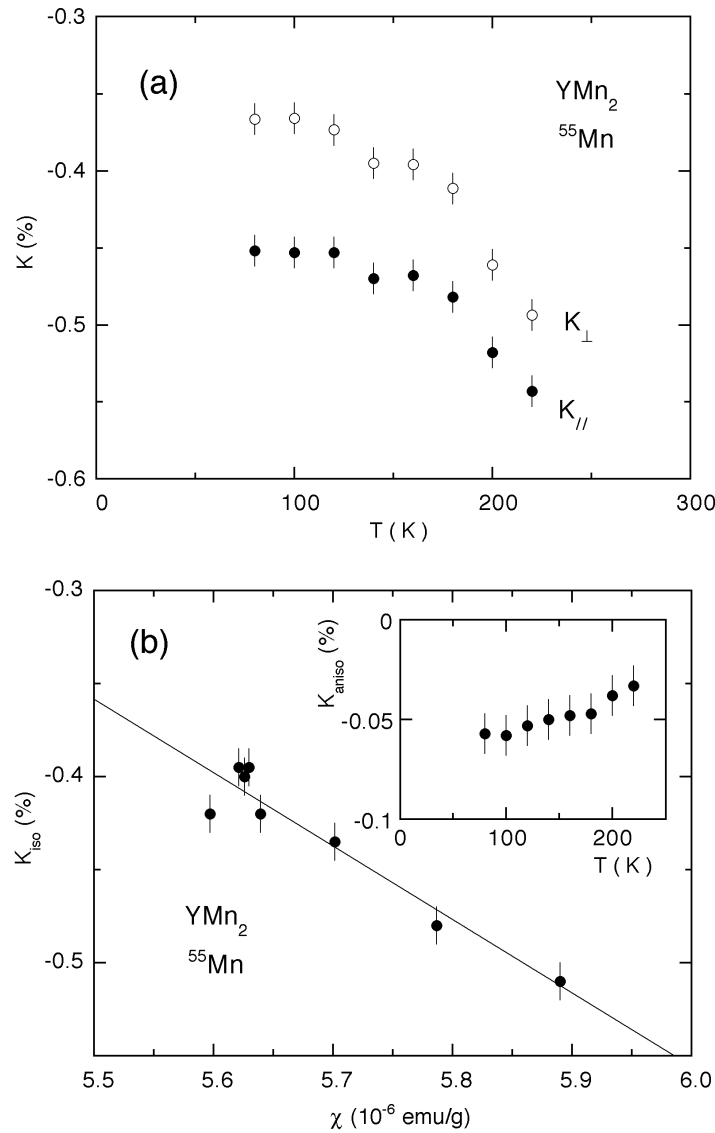


**Figure 5.** (a) Temperature dependences of the Knight-shift components parallel (●) and perpendicular (○) to the symmetry axis for  $\text{YMn}_2$ . The data were measured for the paramagnetic phase in the temperature-decreasing process. (b) A plot of the isotropic Knight shift versus the susceptibility for  $\text{YMn}_2$ . The straight line gives the isotropic hyperfine coupling constant  $A_{\text{iso}} = -22.2 \text{ T } \mu_{\text{B}}^{-1}$ . The inset shows the temperature dependence of the anisotropic Knight shift.

coupling. In figure 5(b), the isotropic component  $K_{\text{iso}} \equiv \frac{1}{3}(K_{\parallel} + 2K_{\perp})$  is plotted against the bulk susceptibility (figure 2(a)) with the temperature being an implicit parameter. The  $K$ - $\chi$  plot is linear, giving the isotropic hyperfine coupling constant  $A_{\text{iso}} = -22.2 \text{ T } \mu_{\text{B}}^{-1}$ , which agrees well with that reported previously by Zheng *et al* [21]. The temperature dependence of the anisotropic Knight shift defined as  $K_{\text{aniso}} \equiv \frac{2}{3}(K_{\parallel} - K_{\perp})$  is shown in the inset of figure 5(b). The anisotropy increases as the temperature approaches the transition point from

higher temperatures. This may be related to the origin of the magnetic transition and/or the symmetry lowering at  $T_N$ . A similar temperature dependence of the anisotropic Knight shift has been observed for another cubic Laves phase compound,  $\text{UMn}_2$ , which shows a structural transition at around 240 K [20]. The appreciable magnitude of the anisotropy observed for  $\text{YMn}_2$  suggests a large orbital contribution to the Knight shift. Assuming isotropy of the hyperfine coupling, the results in figure 5(a) imply that the temperature dependence of  $\chi_\perp$  is larger by about 40% than that of  $\chi_\parallel$ , where  $\chi_\perp$  and  $\chi_\parallel$  are the components of the local susceptibility perpendicular and parallel to the symmetry axis, respectively.

### 3.3. NMR in the magnetically ordered state

The discrepancies among the previous NMR spectra of  $\text{YMn}_2$  may originate from (i) the sample dependence of the NMR spectra (i.e. the sample dependence of the magnetic structure), (ii) insufficiently accurate analyses of the NMR results or (iii) an inappropriate model for the magnetic structure. Here, we will give new comprehensive NMR results for  $\text{YMn}_2$  and explain the reason for the previous disagreement.

Figure 6(a) shows frequency dependences of the spin-echo intensity of  $\text{YMn}_2$  at 4.2 K. The intensity corrections inherent to the apparatus have already been made. These spectra were measured at different values of  $\tau$ , 10 and 50  $\mu\text{s}$ , where  $\tau$  is the time separation between two pulses for the spin-echo experiment. Surprisingly, we obtained markedly different spectral shapes. The profile measured at  $\tau = 10 \mu\text{s}$  has two maxima at around 121 and 134 MHz, which is similar to the result reported by Yoshimura and Nakamura [12] (measured at  $\tau = 15 \mu\text{s}$ ), while the data at  $\tau = 50 \mu\text{s}$  exhibit a single peak with a long tail to the high-frequency side,

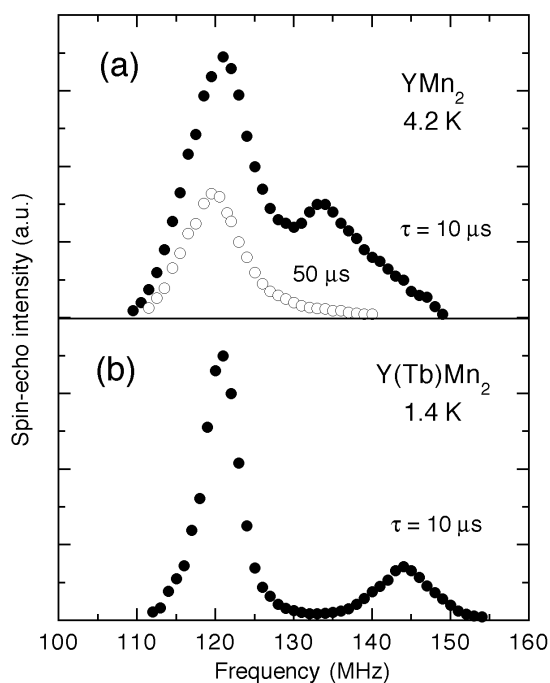


**Figure 6.** Frequency dependences of the  $^{55}\text{Mn}$  spin-echo intensity for  $\text{YMn}_2$  at 4.2 K (a) and  $\text{Y}_{0.97}\text{Tb}_{0.03}\text{Mn}_2$  at 1.4 K (b) with different pulse separations  $\tau$ : 10  $\mu\text{s}$  (●) and 50  $\mu\text{s}$  (○).

which corresponds to the result obtained by Bertier *et al* [13] ( $\tau$  was not given in [13]). These results indicate clearly that the frequency-dependent spin-echo decay time  $T_2$  is the principal origin of the differences among the previous results.

Hence, we measured the spin-echo decay at each frequency. A typical example of the decay curve measured at a frequency of 118 MHz is shown in figure 7 on a semilogarithmic plot. The decay curve  $I(\tau)$  is not of single-exponential type but is roughly described by a stretched exponential function:

$$I(\tau) = I(0) \exp \left[ - \left( \frac{\tau}{T_2} \right)^\beta \right] \quad (3)$$

where  $T_2$  is the tentatively defined transverse relaxation time and  $\beta$  a constant in the range  $0.5 \leq \beta \leq 1$ . The experimental decay can roughly be reproduced with  $\beta = 0.5$ , as shown by the solid curves in figure 7, where the intensity is also plotted against  $\sqrt{\tau}$ . This relation is generally observed when the relaxation times are distributed statistically [22].

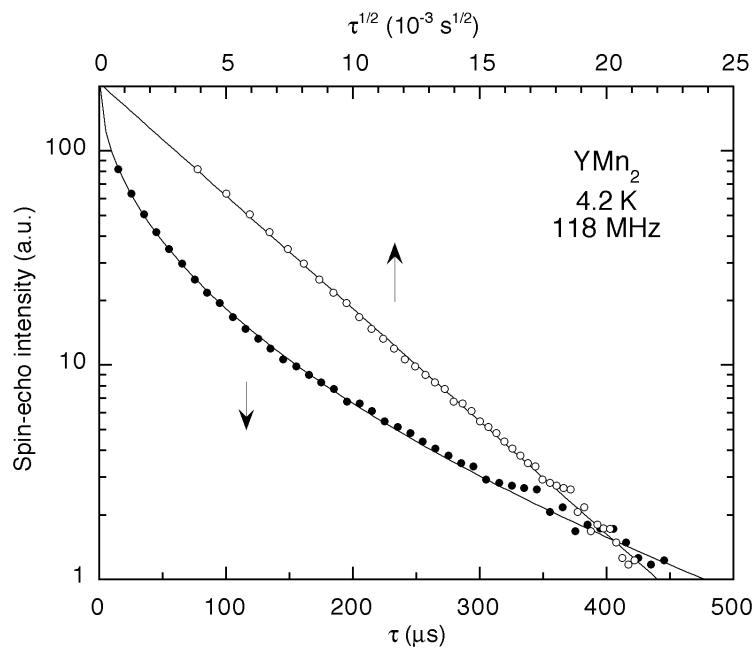


**Figure 7.** The spin-echo decay curve of  $\text{YMn}_2$  measured at 4.2 K and 118 MHz, plotted against  $\tau$  (●) and  $\sqrt{\tau}$  (○). The solid curve indicates the best fit with (3).

Although the shape of the decay curve is slightly dependent on the frequency, we estimated crude values of  $1/T_2$  using equation (3) with fixed  $\beta = 0.5$ . The values obtained are plotted in figure 8(a) as a function of frequency. The relaxation rate  $1/T_2$  shows an unexpectedly large frequency dependence and exhibits a maximum at around the frequency of the high-frequency peak in the spectrum (figure 6(a)). The origin of the distinct frequency dependence will be discussed in section 4.5. The frequency dependence of the transverse relaxation has already been suggested by Bertier *et al* [13] although the effects on the spectral shape were not explicitly discussed. It is notable that the absolute value of  $1/T_2$  depends also on the rf power, i.e. the magnitude of the oscillating field  $H_1$ . This means that the spectral shape measured at a finite  $\tau$  depends also on the rf power. In our measurements, we used a rather large  $H_1$

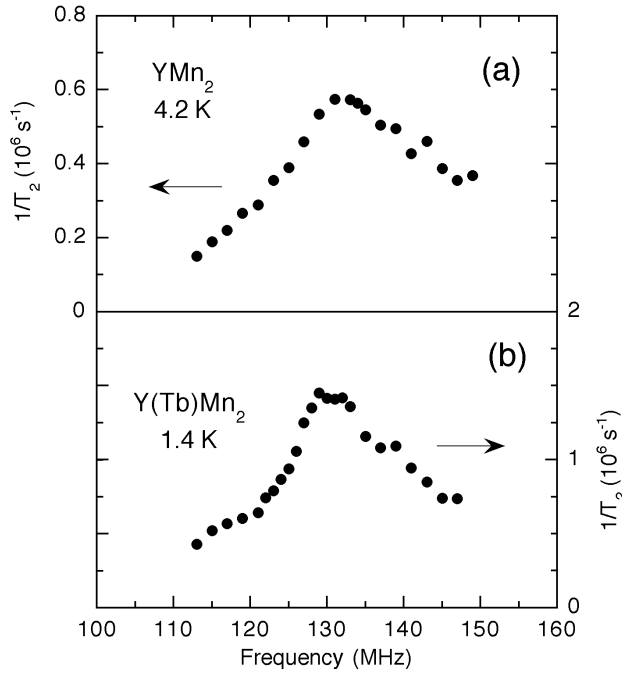


**Figure 8.** Frequency dependences of the spin-echo decay rate  $1/T_2$  (defined in (3)) for YMn<sub>2</sub> at 4.2 K (a) and for Y<sub>0.97</sub>Tb<sub>0.03</sub>Mn<sub>2</sub> at 1.4 K (b).

( $\sim 0.01$  T). Thus the disagreement among the previous results is ascribed to the difference in experimental conditions, particularly as regards  $\tau$  and  $H_1$ , not to sample dependence.

When we discuss the number of atoms which ‘feel’ a certain internal field, we have to deal properly with the observed NMR intensity. It is apparent from the present observation that the frequency dependence of  $T_2$ , which was assumed negligible in previous work, is in fact very significant for YMn<sub>2</sub>. We estimated  $T_2$ -corrected intensities  $I(0)$  by extrapolating the experimental spin-echo decay to  $\tau = 0$  using equation (3). The corrected spectrum is shown in figure 9(a). In addition to the  $T_2$ -correction, the frequency dependence of the intensity enhancement by the rf oscillating field is, in general, important, particularly for anisotropic magnets. For YMn<sub>2</sub>, a slight frequency dependence of the enhancement factor seems to exist, which can be monitored using experimental pulse widths to find the best resonance, but is negligible under the present experimental conditions compared with the distinct frequency dependence of  $T_2$ . As seen in figure 9(a), the second peak at high frequency is enlarged by the  $T_2$ -correction, giving two peaks with almost equal intensity.

It is curious that  $1/T_2$  shows such a strong frequency dependence. Generally, the spin-echo decay rate (homogeneous linewidth),  $1/T_2$ , is dominated by the spin–lattice and spin–spin relaxation mechanisms as follows:

$$\frac{1}{T_2} = \frac{\alpha}{T_1} + \frac{1}{T_2'} \quad (4)$$

where  $T_2'$  is the relaxation time determined by the pure spin–spin relaxation, and  $\alpha$  is a constant depending on the quantum number of the transitions and also on the anisotropy in the local field fluctuation. Here, we call the first and second terms the  $T_1$ -process and  $T_2'$ -process, respectively. To determine the origin of the frequency dependence, we measured  $1/T_1$ . An example of the

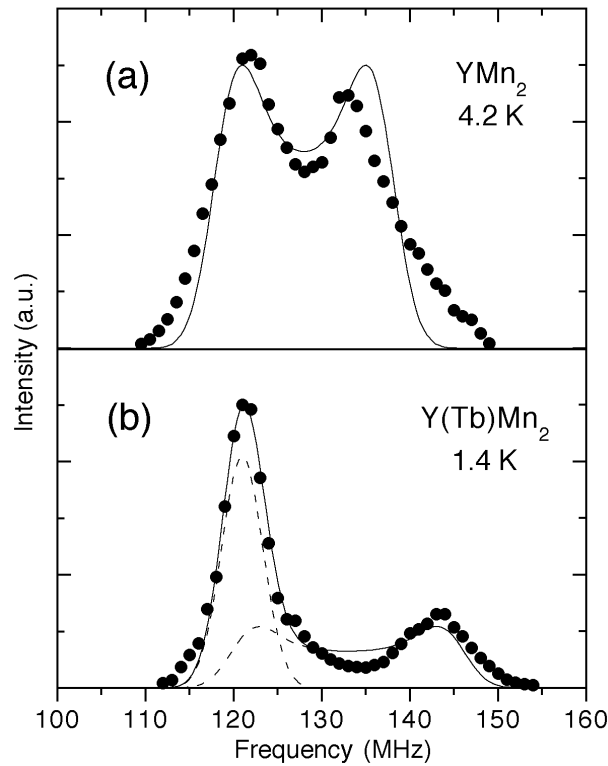


**Figure 9.**  $T_2$ -corrected spectra of  $\text{YMn}_2$  (a) and  $\text{Y}_{0.97}\text{Tb}_{0.03}\text{Mn}_2$  (b). Curves indicate the results calculated assuming spin rotation in the  $\{100\}$  and  $\{111\}$  planes for (a) and (b), respectively. The Gaussian function has been convoluted to take into account the inhomogeneous width. In (b) a 1:1 intensity ratio was assumed for the fixed- $\theta$  ( $\theta = 90^\circ$ ) and distributed- $\theta$  components (see the broken curves and the text).

recovery of the nuclear magnetization, measured at 120 MHz, is shown in figure 10. The recovery curve is not of single-exponential type but is complicated. The non-exponential behaviour is ascribed to the distribution of  $T_1$  and/or the quadrupolar interaction. When the quadrupolar interaction is present, the recovery function of the  $I = \frac{5}{2}$  nuclear magnetization is generally given by the sum of three exponential functions [23]. However, a tentative fitting with the equation for  $I = \frac{5}{2}$  and  $\eta = 0$  failed to reproduce the experimental recovery. Therefore, to take into account the distribution of  $T_1$  similarly to that of  $T_2$ , we fitted the data with a tentative equation:

$$I(t) = I(\infty) \left\{ 1 - \sum_{i=1}^3 c_i \exp \left[ -a_i \left( \frac{\tau}{T_1} \right)^\beta \right] \right\} \quad (5)$$

where  $a_1 = 1$ ,  $a_2 = 6$  and  $a_3 = 15$  for  $I = \frac{5}{2}$  [23]. The weight factors  $c_i$  are in principle established if the initial condition for the nuclear spin system is known, but were treated as free parameters in the present analysis. Similarly to the case for  $T_2$ , an analysis with fixed  $\beta = 0.5$  reproduces the experimental recovery well, as shown by the solid curve in figure 10. The frequency dependence of  $1/T_1$  thus obtained is shown in figure 11. In contrast to the distinct frequency dependence of  $1/T_2$ , only a slight decrease with increasing frequency is shown by  $1/T_1$ . This result indicates that the frequency dependence of  $1/T_2$  is dominated not

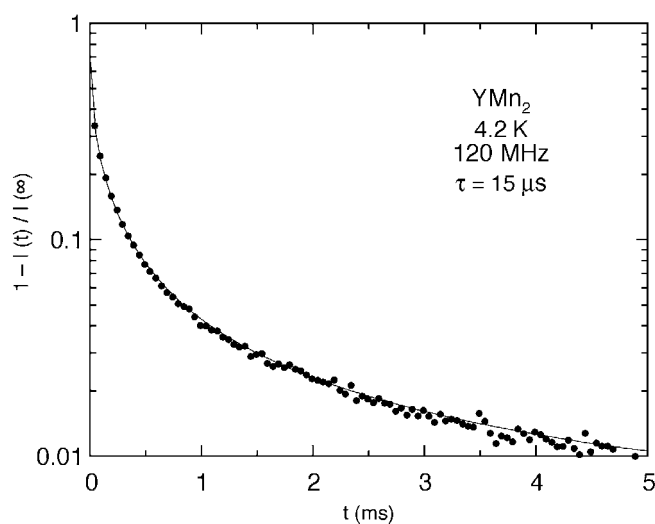


**Figure 10.** The recovery curve of the nuclear magnetization for  $\text{YMn}_2$  measured at 4.2 K, 120 MHz and  $\tau = 15 \mu\text{s}$ . The solid curve is the best fit with (5).

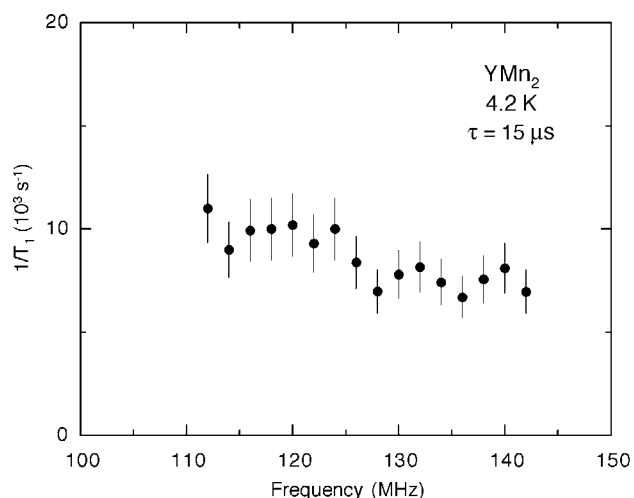


**Figure 11.** The frequency dependence of the nuclear spin-lattice relaxation rate  $1/T_1$  (defined in equation (5)) for  $\text{YMn}_2$  measured at 4.2 K and  $\tau = 15 \mu\text{s}$ .

by the  $T_1$ -process but by the  $T_2$ -process. We also measured the temperature dependence of  $1/T_2$  in the ordered state. Below 20 K, the temperature dependence is very weak or negligible, indicating that the relaxation mechanism of  $1/T_2$  is not based on critical spin fluctuations in the vicinity of the transition point.

We performed similar measurements for  $\text{Y(Tb)Mn}_2$ . Figure 6(b) shows the spectrum measured at  $\tau = 10 \mu\text{s}$ . Since the spin-echo decay is much faster than that of  $\text{YMn}_2$ , we made measurements at a lower temperature, 1.4 K, to obtain an enhanced signal intensity. We obtained a spectrum appreciably different from that of  $\text{YMn}_2$ . The second peak observed for  $\text{YMn}_2$  disappears and, instead, a new peak appears at a higher frequency around 144 MHz. The spin-echo decay is again roughly described by equation (3) with  $\beta = 0.5$ . The frequency

dependence of  $1/T_2$  is shown in figure 8(b); it is quite similar to that for  $\text{YMn}_2$ , in contrast to the marked difference in the lineshape. With the same procedures applied to  $\text{YMn}_2$ , we estimated the  $T_2$ -corrected spectrum, which is shown in figure 9(b). Bertier *et al* [13] made measurements on a sample with a different Tb concentration,  $\text{Y}_{0.9}\text{Tb}_{0.1}\text{Mn}_2$ , and observed only a single peak. They interpreted this as due to the disappearance of the helical modulation associated with the Tb substitution. Our measurements of the high-resolution neutron diffraction for  $\text{Y}_{0.92}\text{Tb}_{0.08}\text{Mn}_2$  [34] indicate that its profile is almost the same as that of  $\text{Y}_{0.97}\text{Tb}_{0.03}\text{Mn}_2$ , i.e. there is still helical modulation along the [110] direction (see section 3.4). Therefore, for  $\text{Y}_{0.9}\text{Tb}_{0.1}\text{Mn}_2$ , the high-frequency peak might be invisible due to  $T_2$  being short.

### 3.4. Neutron diffraction

We summarize and compare the principal results of neutron diffraction experiments for pure  $\text{YMn}_2$  and  $\text{Y(Tb)Mn}_2$ . The results for  $\text{Y(Tb)Mn}_2$  have already been published in [16]. Their results for  $\text{YMn}_2$  are in good agreement with those in the literature [3–5]. Figure 12 shows magnetic diffraction patterns measured by HRPD, which are differences between results obtained at 10 K and room temperature. The peak positions are common to  $\text{YMn}_2$  and  $\text{Y(Tb)Mn}_2$ , indicating that the fundamental magnetic structures are the same. All of the peaks are assigned to Miller indices expected for the fcc type-I structure with  $\vec{Q} = [001]$ . On the other hand, the fine structures of the magnetic peaks are qualitatively different, as shown in figure 13, which shows only the (110) magnetic peaks measured by LTAS. As clearly seen, the (110) peak splits into a doublet and a triplet for  $\text{YMn}_2$  and  $\text{Y(Tb)Mn}_2$ , respectively. These results indicate the modulation of the antiferromagnetic arrangement. Higher-order satellites are not observed, which rules out antiphase structures. According to [3], the doublet

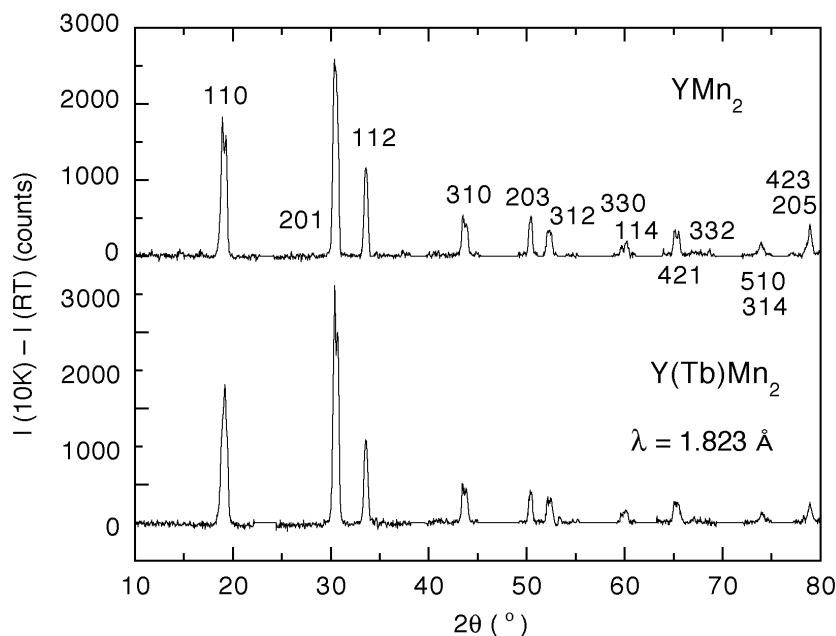


**Figure 12.** Magnetic diffraction patterns for  $\text{YMn}_2$  (a) and  $\text{Y}_{0.97}\text{Tb}_{0.03}\text{Mn}_2$  (b) at 10 K, which are differences between the intensities at 10 K and room temperature measured by HRPD ( $\lambda = 1.823 \text{ \AA}$ ).

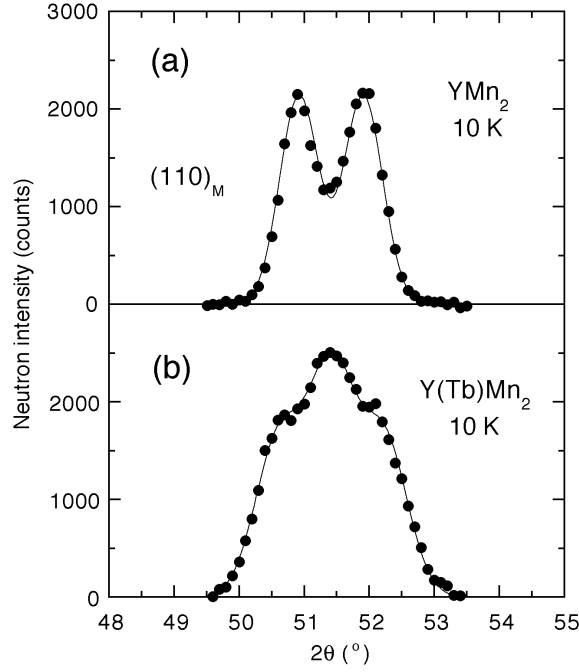


**Figure 13.** The magnetic (110) peaks for YMn<sub>2</sub> (a) and Y<sub>0.97</sub>Tb<sub>0.03</sub>Mn<sub>2</sub> (b) measured at 10 K by LTAS ( $\lambda = 4.750 \text{ \AA}$ ).

corresponds to the helical modulation with  $\vec{Q} = [\tau 01]$ . With the present result at 10 K,  $\tau$  is estimated to be 0.018. On the other hand, for Y(Tb)Mn<sub>2</sub>, the triplet splitting and also the doublet splitting of the (201) peak (see [16]) indicate  $\vec{Q} = [\tau \tau 1]$  with  $\tau = 0.015$ .

Figure 14 shows (222) and (400) nuclear Bragg peaks measured by HRPD at 10 K. The features are common to YMn<sub>2</sub> and Y(Tb)Mn<sub>2</sub>; the (400) peaks splits into two peaks with the intensity ratio 2:1 while the (222) peak remains a single peak, indicating tetragonal lattice distortion below  $T_N$ . The distortion  $1 - c/a$  is estimated to be 0.516 and 0.534% for YMn<sub>2</sub> and Y(Tb)Mn<sub>2</sub>, respectively.

## 4. Discussion

### 4.1. Description of helimagnetic structures

YMn<sub>2</sub> forms the cubic C15-type crystal structure with the space group  $Fd\bar{3}m$ , in which Mn atoms are located at the 16d site. Its site symmetry is trigonal ( $\bar{3}m$ ). The positions  $\vec{r}$  of the 16d site in the unit cell are given by

$$\vec{r} = \left(\frac{5}{8}\frac{5}{8}\frac{5}{8}\right), +\vec{r}_1, +\vec{r}_2, +\vec{r}_3, +\vec{r}_4 \quad (6)$$

with the fcc translation

$$(000)+, \left(0\frac{1}{2}\frac{1}{2}\right)+, \left(\frac{1}{2}0\frac{1}{2}\right)+, \left(\frac{1}{2}\frac{1}{2}0\right)+$$

where

$$\vec{r}_1 = (000) \quad \vec{r}_2 = \left(0\frac{1}{4}\frac{1}{4}\right) \quad \vec{r}_3 = \left(\frac{1}{4}0\frac{1}{4}\right) \quad \vec{r}_4 = \left(\frac{1}{4}\frac{1}{4}0\right). \quad (7)$$

In other words, the 16d site is divided to four fcc Bravais sublattices.

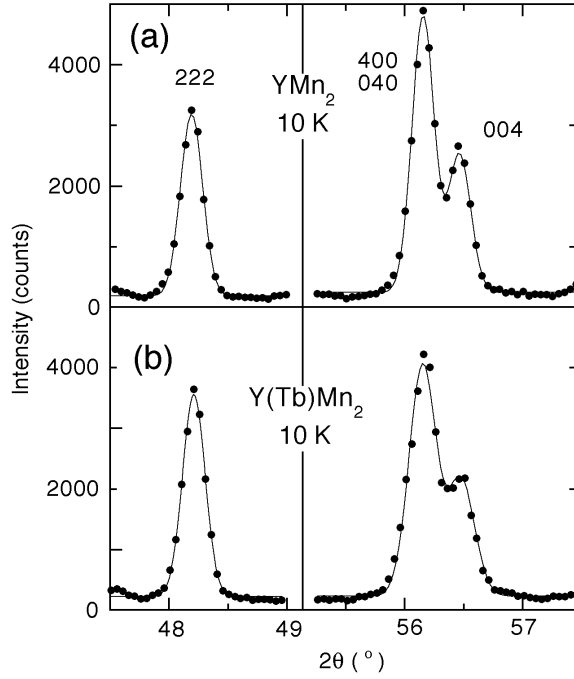


**Figure 14.** The nuclear peaks, (222) and (400), for  $\text{YMn}_2$  (a) and  $\text{Y}_{0.97}\text{Tb}_{0.03}\text{Mn}_2$  (b) measured at 10 K by HRPD ( $\lambda = 1.823 \text{ \AA}$ ).

For simplicity, we treat separately the spin configuration for one of the fcc sublattices and the mutual relations among the four sublattices. The magnetic moment at the position  $\vec{r}$  in a helimagnetic fcc sublattice is described by

$$\vec{m}(\vec{r}) = m \left[ \vec{u} \cos(\vec{Q} \cdot \vec{r}) + \vec{v} \sin(\vec{Q} \cdot \vec{r}) \right] \quad (8)$$

where  $m$  gives the magnitude of the moment,  $\vec{u}$  and  $\vec{v}$  are mutually orthogonal unit vectors. The phase shift is omitted for simplicity. The position  $\vec{r}$  and the propagation vector  $\vec{Q}$  are taken in units of the unit lattice vectors and the unit reciprocal-lattice vectors, respectively;  $\vec{r} = x\vec{a} + y\vec{b} + z\vec{c} = (xyz)$  and  $\vec{Q} = 2\pi(h\vec{a}^* + k\vec{b}^* + l\vec{c}^*) = 2\pi(hkl) \equiv [hkl]$ . The observed magnetic reflections (110), (201), (112), (310), (203), (312) etc (see figure 12) are included in those expected for  $\vec{Q} = [001]$ . As mentioned in section 3.4, the neutron diffraction results indicate  $\vec{Q} = [\tau 01]$  and  $[\tau \tau 1]$  for  $\text{YMn}_2$  and  $\text{Y(Tb)Mn}_2$ , respectively, where  $\tau$  corresponds to the inverse of the period in units of the lattice parameter  $a$ . The much longer modulation along the [010] direction suggested by Cywinski *et al* [4] will be neglected for simplicity in the following discussion.

It may be convenient to define another propagation vector  $\vec{q}$  to describe the mutual spin directions among the four sublattices. Assuming that all four fcc sublattices have the same helical axis, i.e. the same  $\vec{u}$  and  $\vec{v}$ , the fundamental spin configuration in a unit tetrahedron is described by

$$\vec{s}_i (\equiv \vec{m}(\vec{r}_i)) = \vec{m}_0 \exp(-i\vec{q} \cdot \vec{r}_i) \quad (i = 1, 2, 3, 4) \quad (9)$$

where  $\vec{m}_0$  gives the magnitude and direction of the moment. In the neutron diffraction patterns, some of the peaks expected for the fcc type-I structure were not observed: (001), (003)/(221),

(401)/(223), (005)/(403) etc. With the restriction (1) and  $\vec{Q} = [001]$ , this condition is fulfilled in the case of  $\vec{q} = [200]$ .

On the introduction of inhomogeneity, the helical axis is changed from [100] to [110]. Let us consider this transition in more detail. If we introduce helical modulation along the [100] direction (the  $a$ -axis), the phase of the modulation  $\psi$  at the position  $(x, y)$  obeys  $\psi \propto x$  (or  $\psi \propto y$ ). This means that the phase varies (the spin direction rotates) in both the [110] and  $[1\bar{1}0]$  chains. When the modulation is along the [110] direction,  $\psi \propto x + y$ . This implies that all spins in a  $[1\bar{1}0]$  chain have a constant  $\psi$ , i.e. the spins rotate only in the [110] chains and are locked in collinear arrangements in the  $[1\bar{1}0]$  chains. This means that the [110] and  $[1\bar{1}0]$  chains are no longer equivalent. Therefore, the switching of the modulation direction from [100] to [110] induced by the Tb substitution is a symmetry lowering (phase transition) from the isotropic helical modulation to an asymmetric one. In fact, this transition is accompanied by switching of the spin-rotation plane, as seen in the next section.

#### 4.2. Helimagnetism observed by means of NMR: analysis assuming single-axial states

We discuss the directions of the moments, i.e. the spin-rotation planes in the helimagnetic states, mainly on the basis of the NMR results. The Mn site (the 16d site) has an axial symmetry along one of the  $\langle 111 \rangle$  axes. Note that there are four kinds of *local* symmetry axes as shown in figure 15(a). It was confirmed by a lattice point charge calculation that the directions of the local symmetry axes are scarcely modified by the small lattice distortion below  $T_N$ . Therefore, the tetragonal distortion below  $T_N$  can be neglected in the NMR analysis. When the hyperfine field is anisotropic, the resonance frequency  $\nu = \gamma H_{\text{loc}}$  is written in a first approximation as

$$\nu(\theta) = \nu_0 + \frac{1}{2}\nu_1(3\cos^2\theta - 1) \quad (10)$$

where  $\nu_0$  and  $\nu_1$  are parameters corresponding to the angle-independent and angle-dependent components of the hyperfine field, and  $\theta$  is the angle between the magnetic moment and the local symmetry axis. In this model, the distribution of  $\theta$  causes a broadening of the NMR spectrum. For simplicity, we neglect the nuclear quadrupole interaction, although a small quadrupole splitting ( $\nu_Q \simeq 2.6$  MHz) was observed in the paramagnetic state. We treat equation (10) phenomenologically and do not deal with the microscopic origin of the hyperfine interaction.

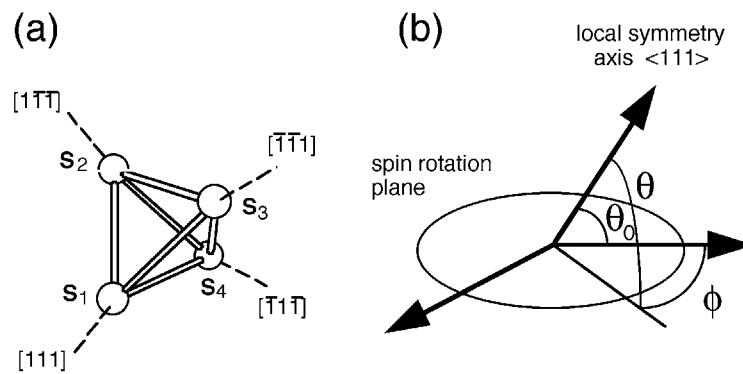


**Figure 15.** (a) Local symmetry axes (---) of the atomic sites in a tetrahedron. (b) The general relation between the local symmetry axis (one of the  $\langle 111 \rangle$  axes) and the spin-rotation plane, and the definition of  $\theta$  and  $\phi$ . The minimum of  $\theta$ ,  $\theta_0$ , depends on the relative orientation of the symmetry axis and the spin plane.

We calculate the NMR spectra by assuming a homogeneous distribution of the spin directions. As the simplest case, we assume that the helical axis and plane are the same for all of the fcc sublattices. To calculate the lineshape, it is necessary to know the relation between  $\theta$  and the angle of the spin in the rotation plane,  $\phi$  (measured from a certain direction in the plane). The general relation between the spin direction and the symmetry axis (one of the  $\langle 111 \rangle$  ones) is schematically shown in figure 15(b), where  $\theta$  is distributed between the minimum angle  $\theta_0$  and  $90^\circ$ , and  $\theta_0$  depends on the relative orientation of the spin-rotation plane and the local symmetry axis, resulting in different spectral widths and singular points. For a homogeneous distribution of  $\phi$ , the lineshape is given by  $I(\nu) \propto (d\nu(\phi)/d\phi)^{-1}$ . In figure 16 we show typical examples of the spectra thus calculated for the spin rotations in typical highly symmetric planes of the cubic lattice,  $\{100\}$ ,  $\{110\}$  and  $\{111\}$ . The corresponding angle  $\theta$  is also shown at the top of the figure. It should be noted that, in some cases, the relation between  $\theta$  and  $\phi$  is not unique, since there are four kinds of local symmetry axis. The sketches on the right-hand side in figure 16 display the relations between the spin-rotation planes (ellipsoids) and the local symmetry axes (broken lines).

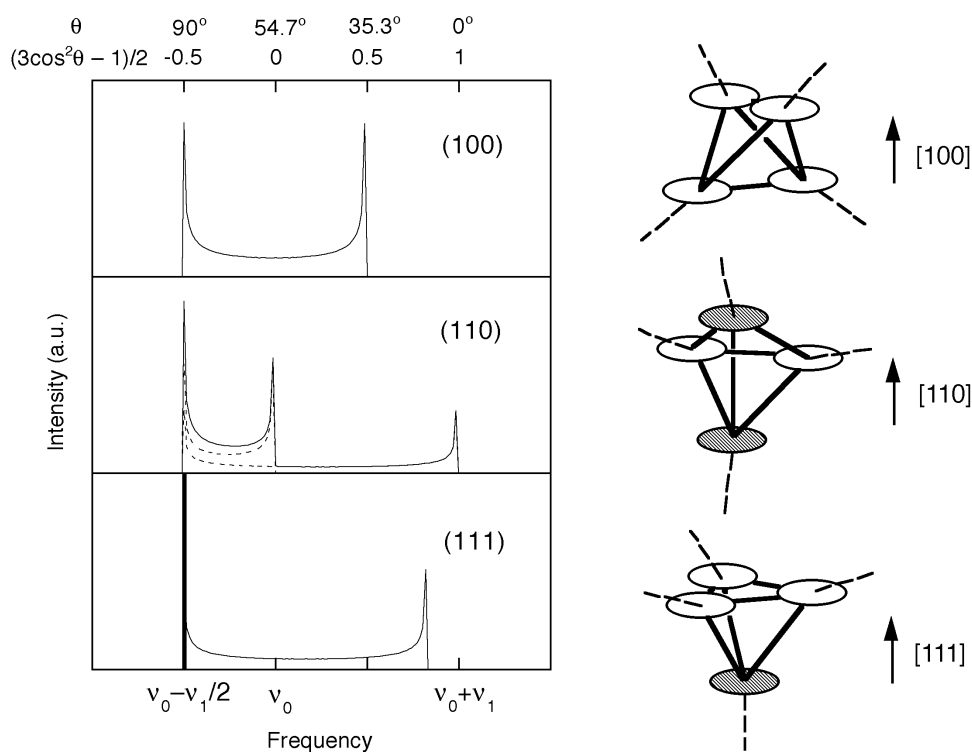


**Figure 16.** Calculated NMR spectra assuming homogeneous and single-axial helimagnetic modulation with the spin rotation in  $\{100\}$ ,  $\{110\}$  and  $\{111\}$  planes. The sketches on the right-hand side show the relative orientations of the spin-rotation planes (ellipsoids) and the local symmetry axes (---). Open and hatched ellipsoids represent different types (see the text).

For the  $\{100\}$ -plane rotation, we have  $\cos \theta = (\sin \phi + \cos \phi)/\sqrt{3}$ , where  $\phi$  is measured from the  $[001]$  axis. The spectrum has two peaks, at  $\nu_0 - \frac{1}{2}\nu_1$  and  $\nu_0 + \frac{1}{2}\nu_1$ , with equal intensity.

For the  $\{110\}$ -plane rotation, there are two kinds of local  $\langle 111 \rangle$  axis with respect to the  $(110)$  plane: (i)  $\langle 111 \rangle$  axes within the  $(110)$  plane, i.e.  $[\bar{1}11]$  and  $[1\bar{1}1]$ , and (ii)  $\langle 111 \rangle$  axes not included

in the (110) plane, i.e.  $[111]$  and  $[\bar{1}\bar{1}1]$ . For (i) and (ii), we have  $\cos \theta = (\sqrt{2} \sin \phi + \cos \phi) / \sqrt{3}$  and  $\cos \theta = \cos \phi / \sqrt{3}$ , respectively, with  $\phi$  measured from the  $[001]$  axis. The lineshape is given by the superposition of two different doublets with different splittings. Since one of the singular points is the same for both doublets, a spectrum with three maxima at  $\nu_0 - \frac{1}{2}\nu_1$ ,  $\nu_0$  and  $\nu_0 + \frac{1}{2}\nu_1$  with different intensities is obtained.

For the  $\{111\}$ -plane rotation, there are two kinds of site with (i)  $\cos \theta = 0$  ( $[111]$ ) and (ii)  $\cos \theta = 2\sqrt{2} \cos \phi / 3$  ( $[\bar{1}\bar{1}1]$ ,  $[1\bar{1}1]$  and  $[\bar{1}\bar{1}\bar{1}1]$ ), where  $\phi$  is measured from the  $[121]$  axis, with the population ratio 1:3. The spectrum consists of a delta function at  $\nu_0 - \frac{1}{2}\nu_1$  for case (i) and a doublet with maxima at  $\nu_0 - \frac{1}{2}\nu_1$  and  $\nu_0 + \frac{5}{6}\nu_1$  for case (ii), resulting in a double-peak structure with the peaks having different intensities.

Assuming the hyperfine mechanism to be common to  $YMn_2$  and  $Y(Tb)Mn_2$ , qualitative comparison between the experimental  $T_2$ -corrected spectra (figure 9) and the calculated profiles (figure 16) indicates that spins rotate in the  $\{100\}$  and  $\{111\}$  planes in  $YMn_2$  and  $Y(Tb)Mn_2$ , respectively. The disagreement in fine structure is insignificant since the above calculations were simplified in various steps. The parameters are estimated as  $\nu_0 = 128$  and  $130$  MHz for  $YMn_2$  and  $Y(Tb)Mn_2$ , respectively, and  $\nu_1 = 18$  MHz for both. On the other hand, the neutron diffraction intensity analysis is not so effective for discerning the spin-rotation plane (except in specific cases) because the angle factor is more or less averaged out in the helimagnetic states. We calculated the magnetic reflection intensities assuming only (100)- and (111)-plane spin rotations and found that the accordance between the calculated and experimental results is satisfactory for both  $YMn_2$  and  $Y(Tb)Mn_2$ .

In fact, however, there seems to be quantitative disagreement as regards the spectrum analysis for  $Y(Tb)Mn_2$ . As discussed above, we expect a 1:3 population ratio for the fixed- $\theta$  ( $\theta = 90^\circ$ ) component and the distributed- $\theta$  doublet. In contrast to this, an analysis of the integrated intensity favours 1:1. In figure 9(b), the Gaussian-convoluted spectrum taking into account the inhomogeneous width (the full width of 5.5 MHz) is shown by broken curves for each part and by the solid curve for the total, assuming the 1:1 population ratio. This inconsistency may be resolved by assuming a double-axial helical modulation as discussed below.

#### 4.3. Possibility of double-axial states

Although the origin of the tetragonal distortion observed below  $T_N$  is not explicit, it is reasonable to at least expect it to be related to the magnetic symmetry. In section 4.2, we showed that the  $\{100\}$ -plane spin rotation is consistent with the NMR spectrum of  $YMn_2$ . For the simple proper screw structure, however, the best fit to neutron diffraction intensities is obtained for spin rotation in the (100) plane, not in the (001) plane. It is difficult to correlate this model with the distortion along the  $[001]$  direction. In this section, we try to find the spin structures that are consistent with this crystal symmetry. Our basic assumptions are the following:

- (i) We believe that the tetragonal distortion originates primarily from the partial release of the frustration. That is, we restrict our models to ones with antiparallel spin arrangements in the  $[110]$  and  $[1\bar{1}0]$  chains, but assume rather arbitrary coupling between (001) planes.
- (ii) Even if the primary origin of the crystal distortion is the reduction of the magnetic dimensionality, the final tetragonal symmetry should be of great significance and suggests that the directions of spins should also show tetragonal symmetry.

In addition, the common lattice symmetry of  $YMn_2$  and  $Y(Tb)Mn_2$ —in spite of the different modulation directions—suggests a *local* nature of the lattice distortion.

The basic idea is to recognize  $\text{YMn}_2$  as a weakly coupled assembly of one-dimensional antiferromagnetic spin chains, and the aim is to find the magnetic structures which satisfy the above condition and explain the experimental results from the neutron diffraction and NMR investigations. Although Vokhnyanin *et al* [5] approached this problem from a different point of view, their model does not satisfy the above conditions; the elemental unit in the model (see figure 3 in [5]) is coupled antiparallel along  $[101]$  and  $[10\bar{1}]$  and decoupled along  $[010]$ , and its local symmetry is lower than tetragonal. Therefore we will not consider their model further.

We start from *local* symmetry consideration. The tetragonal symmetry implies the presence of two independent and equivalent  $\vec{q}$ -vectors of  $\{200\}$ , i.e.  $\vec{q}_1 = [200]$  and  $\vec{q}_2 = [020]$ . Thus the relation (9) can be replaced by the double- $\vec{q}$  state described by

$$\vec{s}_i = \vec{m}_1 \exp(-i\vec{q}_1 \cdot \vec{r}_i) + \vec{m}_2 \exp(-i\vec{q}_2 \cdot \vec{r}_i) \quad (i = 1, 2, 3, 4). \quad (11)$$

It is now enough to select appropriate  $\vec{m}_1$  and  $\vec{m}_2$  to determine the mutual spin directions among the four sublattices. Within condition (2),  $\vec{m}_1$  and  $\vec{m}_2$  should be mutually orthogonal vectors. The antiparallel coupling in the  $[110]$  and  $[1\bar{1}0]$  chains is described by

$$\vec{s}_1 = -\vec{s}_4 \quad \text{and} \quad \vec{s}_2 = -\vec{s}_3 \quad (12)$$

for the elemental unit. Typical examples of double- $\vec{q}$  states which satisfy (1), (2) and (12) are shown in figure 17 together with the corresponding single- $\vec{q}$  states. As seen in the figure, the double- $\vec{q}$  states (c) and (d) have  $\pi/2$  rotational symmetry on the projected  $c$ -planes. Although the frustration is partially released in the tetragonal symmetry, these spin structures are still degenerate in energy. Therefore a secondary and minor interaction other than the simple spin-spin interaction should determine the spin direction.

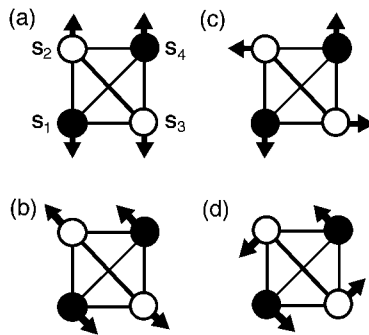


**Figure 17.** Examples of local spin configurations in the unit tetrahedron ( $\bullet$ :  $z = 0$ ;  $\circ$ :  $z = \frac{1}{4}$ ). The  $c$ -axis is perpendicular to the surface. (a) and (b) are single- $\vec{q}$  states, and (c) and (d) are double- $\vec{q}$  states with local tetragonal symmetry.

In actual helimagnetic structures, the double  $\vec{q}$  implies that the  $[110]$  and  $[1\bar{1}0]$  spin chains have different helical axes, i.e. different  $\vec{u}$  and  $\vec{v}$ . The double-axial model considered for  $\text{YMn}_2$  is shown schematically in figure 18, where the elemental unit is given by figure 17(c) and spins rotate in the  $(100)$  and  $(010)$  planes in the  $[110]$  and  $[1\bar{1}0]$  chains, respectively. This is obtained by modifying the model proposed by Ballou *et al* [3] by changing the spin-rotation plane of the  $[1\bar{1}0]$  chain from  $(100)$  to  $(010)$ . For  $\text{Y(Tb)Mn}_2$  we modify this structure by tilting the spin-rotation planes away from  $\{100\}$  planes (and locking the phase of the spins in the  $[1\bar{1}0]$  chains):  $(111)$  or  $(11\bar{1})$  for the  $[110]$  chains and  $(1\bar{1}1)$  or  $(1\bar{1}\bar{1})$  for the  $[1\bar{1}0]$  chains (see figure 19(b)). The stability of these structures will be discussed in the next section.

How can we discriminate experimentally between these single- and double-axial structures? NMR as a local probe is effective in some cases. Let us discuss  $\text{Y(Tb)Mn}_2$  first.

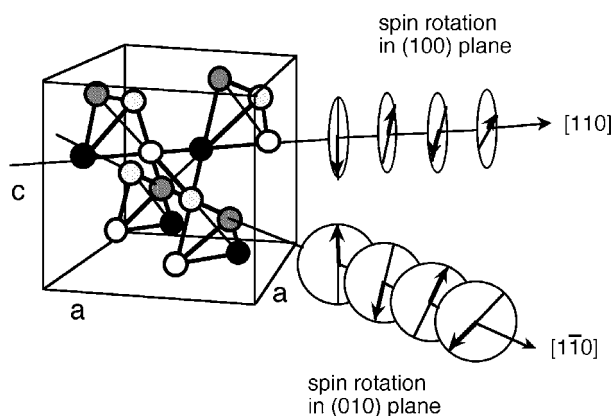


**Figure 18.** The schematic representation of the double-axial helimagnetic structure considered for  $YMn_2$ . Spins rotate helically in (100) and (010) planes in  $[110]$  and  $[1\bar{1}0]$  spin chains, respectively.

It is easily found that the NMR spectra are different for the single- and double-axial states. Figure 19 shows simplified sketches of the single- and double-axial states, where ellipsoids represent the  $\{111\}$  spin-rotation planes and broken lines the  $\langle 111 \rangle$  local symmetry axes. As discussed in section 4.2, there are two different types of site as regards the orientation between the local symmetry axis and the spin-rotation plane. One is (i) the case where the symmetry axis is always perpendicular to the spin-rotation plane (hatched ellipsoids) and the other is (ii) the case with the spin direction  $\theta$  distributed over the range  $19.5\text{--}90^\circ$  (open ellipsoids). As seen in figure 19(b), in *both* the  $[110]$  and  $[1\bar{1}0]$  chains half of the Mn spins have  $\theta = 90^\circ$  in

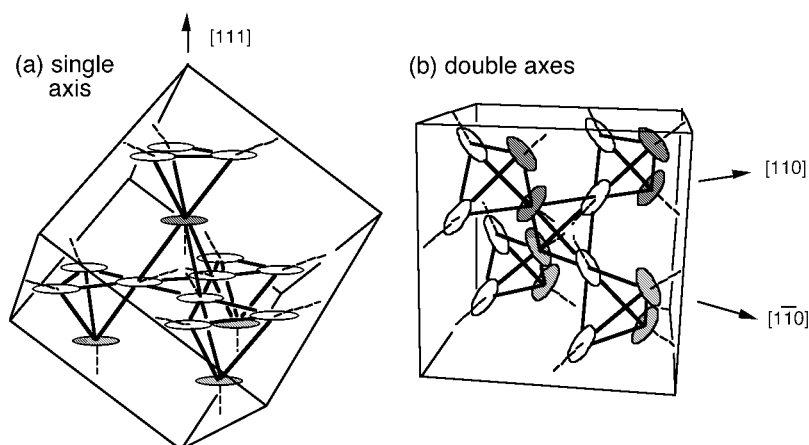


**Figure 19.** Simplified sketches of the single-axial (a) and double-axial structures (b) considered for  $Y(Tb)Mn_2$  (the  $\{111\}$ -plane spin rotation). Ellipsoids and broken lines represent the  $\{111\}$  spin-rotation planes and the  $\langle 111 \rangle$  local symmetry axes, respectively. Open and hatched ellipsoids represent different types, where the angle  $\theta$  is fixed at  $90^\circ$  and distributed in the range  $19.5\text{--}90^\circ$ , respectively. In the single-axial structure, where all spin-rotation planes are the same (111) plane, the population ratio of the fixed- $\theta$  and distributed- $\theta$  components is 3:1. On the other hand, the double-axial states have different spin-rotation planes for the  $[110]$  and  $[1\bar{1}0]$  chains, resulting in a 1:1 ratio of the fixed- $\theta$  and distributed- $\theta$  components.

the double-axial structure. Therefore, the population ratio of the cases (i) and (ii) is 1:1 for the double-axial state, which is different from 1:3 for the single-axial state. As was pointed out in section 4.2, the intensity analysis of the experimental spectrum (figure 9(b)) favours 1:1, suggesting that the double-axial state is realized in Y(Tb)Mn<sub>2</sub>.

On the other hand, for pure YMn<sub>2</sub>, the single- and double-axial states of the {100} spin rotation give the same NMR spectrum, because the relative orientation of the {100} planes and the <111> local symmetry axes is unique and independent of the dimension. In addition, the neutron diffraction patterns for the double-axial state and the corresponding single-axial one (including the helical modulation) are the same if the latter state is composed of multi-domains with equal populations. Therefore, we cannot discriminate between these states.

#### 4.4. The origin of the spin reorientation and the helical modulation

First, note that the single-ion anisotropy of the Tb moments does not directly contribute to the spin reorientation because they behave paramagnetically down to low temperature. Generally the direction of the spins is determined by the exchange interaction and the anisotropy (which, here, includes not only single-ion anisotropy but also anisotropic or higher-order exchange interaction). The former favours simpler or more highly symmetric structures and the latter makes the spins orient in the easy-magnetization direction. Some experimental results indicate strong magnetocrystalline anisotropy in YMn<sub>2</sub>, probably via the spin-orbit coupling. The Knight-shift anisotropy in the paramagnetic state is large. In the ordered state, the anisotropy in the internal field plays a principal role in determining the NMR spectra and the relaxation times (as will be discussed in section 4.5). Ballou *et al* [8] suggested that the easy plane of the magnetization for each Mn atom is perpendicular to the local symmetry axis from referring to the spin-reorientation process observed in NdMn<sub>2</sub>. Taking into account these results, we assume that the Mn spins tend to orient perpendicular to the local symmetry axes. In addition to this easy-plane anisotropy, we assume that, as already emphasized, the antiparallel configuration is preferred in the [110] and [1 $\bar{1}$ 0] chains. In this case, the structure of Y(Tb)Mn<sub>2</sub> is understandable, where spins—as many as possible—orient perpendicular to the local symmetry axis while conserving the antiparallel coupling in the [110] and [1 $\bar{1}$ 0] chains. It is clear that the double-axial structure is preferable to the single-axial one from considering the anisotropy energy. In fact, Ballou *et al* [8] have already discussed a similar double-axial state as a possible structure for pure YMn<sub>2</sub>. On the other hand, the double-axial structure suggested here for YMn<sub>2</sub> has tetragonal symmetry not only locally but also over a long range. All the spin-rotation planes are equivalent with respect to their local symmetry axes. The helical modulation is isotropic, in contrast to the partly locked collinear spin chains in Y(Tb)Mn<sub>2</sub>. This is the so-called proper screw structure, in which the helical axes are perpendicular to the spin-rotation planes. Thus the spin reorientation caused by the substitution of a small amount of Tb is interpreted as the symmetry lowering (phase transition) from the coherent state to an asymmetric but locally preferable configuration as a result of the loss of the delicate balance between the exchange interaction and the anisotropy. In actual substances, it is likely that these two states coexist to some extent due to the presence of slight inhomogeneity or impurity. This may explain the much more extended helical modulation in the *b*-direction [4] and some sample dependences reported previously.

The origin of the long-period helical modulation has not been discussed explicitly. Terao [30] discussed the magnetic structure of this lattice taking into account up to third-neighbour interactions and claimed that no helical modulation appears. One hint, from the discussion on the fcc lattice, which is another three-dimensional fully frustrated system, is suggestive. Giebultowicz *et al* [31] argued that an incommensurate helical modulation is

induced by the (artificial) tetragonal distortion in the type-I fcc antiferromagnet. They took into account nearest-neighbour and next-nearest-neighbour interactions,  $J_1$  and  $J_2$ , and assumed the separation of  $J_1$  into  $J_\perp$  and  $J_\parallel$  as a result of the tetragonal distortion, where  $\perp$  and  $\parallel$  indicate components perpendicular and parallel to the  $c$ -axis, respectively. In this model, the tilt angle of the spins,  $\psi$ , is given by  $\cos \psi = (J_\perp - J_\parallel)/J_2$ . Since the corner-sharing tetrahedral lattice consists of four fcc sublattices, this model may be applied to YMn<sub>2</sub>. In the NSK structure, interactions from up to fifth-neighbour spins cancel due to the antiferromagnetic coupling. The effective  $J_2$  is the interaction with a sixth neighbour at a distance  $9a/8$ , which may be small with respect to  $J_\perp - J_\parallel$ , resulting in a long-period modulation. If this is the case, one expects the helix period to depend on the distortion. We actually observed a correlation between the temperature-dependent distortion and the period measured for YMn<sub>2</sub> [18, 33] although Ritter *et al* [32] claimed to find no correlation in a comparison of some pseudobinary systems. In this scenario, the long-period modulation originates from the small distortion induced to release the frustration in the corner-sharing tetrahedral lattice.

#### 4.5. Angle dependence of the relaxation time

In the magnetically ordered states of YMn<sub>2</sub> and Y(Tb)Mn<sub>2</sub>, the spin-echo decay time  $T_2$  depends strongly on the frequency. This feature being common to YMn<sub>2</sub> and Y(Tb)Mn<sub>2</sub>, in spite of the difference in lineshape, suggests that  $T_2$  depends on the angle between the internal fields and the crystallographic axis, i.e.  $\theta$ . One of the characteristic features is that the shortest  $T_2$  is at  $\theta \simeq 45^\circ$ . This rules out the possibility of the spin-diffusion mechanism being the origin of the frequency-dependent  $T_2$ , which is frequently present for inhomogeneously broadened lines.

Generally, the relaxation phenomena are described by the Fourier transform of the fluctuating local field  $\delta H_{\text{loc}}(t)$ . The characteristic times  $T_1$  and  $T_2'$  for the  $T_1$ - and  $T_2$ -processes, respectively, are given by

$$\begin{aligned} \frac{1}{T_1} &= \frac{\gamma^2}{2} \int_{-\infty}^{\infty} \langle \{\delta H_+(t), \delta H_-(0)\} \rangle \exp(i\omega t) dt \\ \frac{1}{T_2'} &= \frac{\gamma^2}{2} \int_{-\infty}^{\infty} \langle \{\delta H_z(t), \delta H_z(0)\} \rangle dt \end{aligned} \quad (13)$$

where  $\omega$  is the resonance frequency,  $\delta H_\pm = \delta H_x \pm i\delta H_y$  and  $\{A, B\} = \frac{1}{2}(AB + BA)$  [24].  $\langle \rangle$  means the statistical average. Thus  $T_2'$  is determined by fluctuations of local fields along the quantization ( $z$ -) axis, while  $T_1$  is described by those perpendicular to the  $z$ -axis. The lack of distinct angle dependence of  $T_1$  indicates clearly that the characteristic features of  $T_2$  are dominated by the  $T_2$ -process. The most basic mechanism of the  $T_2$ -process is the direct dipolar coupling between like nuclei. This interaction is weak, particularly in the magnetically ordered state with an inhomogeneously broadened spectrum. The indirect interaction via conduction electrons—the so-called Ruderman–Kittel interaction [25]—is expected to be angle independent. One well-known relaxation mechanism in the magnetically ordered state is the indirect interaction via electron spin waves—the Suhl–Nakamura interaction [26, 27]. If there is an anisotropy in the spin-wave excitations, this interaction may be angle dependent. In this case, however, we expect a more distinct angle dependence in the  $T_1$ -process and the largest  $T_2$  at the magic angle ( $3 \cos^2 \theta - 1 = 0$ ). Since the Suhl–Nakamura interaction depends on the quantum number of the transitions [28], a large quadrupolar interaction may result in an angle-dependent  $T_2$ , but not in the present case.

Here, we introduce a simple phenomenological model just for qualitative discussion. We attribute the relaxation to time-dependent local fields associated with the dynamic motion of

electron spins. Since moment directions distribute spatially with respect to the crystallographic axis, the directional fluctuations result in an angle dependence of the time-dependent local field. Here the time-averaged local field is given by  $H_{\text{loc}} = \nu/\gamma$  with  $\nu$  as in equation (10). If  $H_{\text{loc}}$  changes its magnitude to  $H_{\text{loc}} + \delta H_{\text{loc}}^{\parallel}(t)$  when the angle  $\theta$  fluctuates to  $\theta + \delta\theta(t)$ , the longitudinal fluctuations  $\delta H_{\text{loc}}^{\parallel}(t)$  are given by

$$\delta H_{\text{loc}}^{\parallel}(t) = \frac{dH_{\text{loc}}}{d\theta} \delta\theta(t). \quad (14)$$

Referring to the relaxation rate in equation (13), which is proportional to the square of the field, we have

$$\frac{1}{T_2'} \propto \delta H_{\text{loc}}^{\parallel}(t)^2 \propto \nu_1^2 \sin^2 2\theta \quad (15)$$

where we have assumed that  $\delta\theta(t)$  does not depend on  $\theta$ . In this case  $1/T_2'$  has a maximum at  $\theta = 45^\circ$  and minima at  $\theta = 0$  and  $90^\circ$ . A similar argument for  $T_2$  has already been applied to some materials by Abelyashev *et al* [29].

On the other hand, transverse fluctuations of the local field are produced by angular motion both in  $\theta$  and  $\phi$ , where  $\phi$  is the angle in the plane perpendicular to the local symmetry axis. In the case of the easy-plane anisotropy in the plane perpendicular to the local symmetry axis, we expect fluctuations in  $\phi$  to dominate over the transverse fluctuations, which may be approximated as  $\delta H_{\text{loc}}^{\perp}(t) \sim H_{\text{loc}} \sin \theta \delta\phi(t)$ . Then, we have

$$1/T_1 \propto \delta H_{\text{loc}}^{\perp}(t)^2 \propto \left[ \nu_0 + \frac{1}{2} \nu_1 (3 \cos^2 \theta - 1) \right]^2 \sin^2 \theta$$

which decreases monotonically against frequency ( $\propto 3 \cos^2 \theta - 1$ ); this is consistent with the experimental result (figure 11). Taking into account equation (4), the calculated frequency dependence of  $1/T_2$ , including the asymmetry against frequency, agrees well with the experimental result (figure 8). Hence the phenomenological model successfully explains the angle dependences of the relaxation times.

Finally, we comment on the magnitude of the hyperfine coupling constant. In the analysis in section 4.2, the angle-independent part of the internal field was estimated to be  $H_{\text{iso}} = \nu_0/\gamma \simeq 12.3$  T. With the ordered moment  $2.7 \mu_{\text{B}}$ , the isotropic hyperfine coupling constant is calculated as  $|A_{\text{AF}}| = 4.6 \text{ T } \mu_{\text{B}}^{-1}$ . On the other hand, the isotropic coupling constant in the paramagnetic state is  $A_{\text{P}} = -22.2 \text{ T } \mu_{\text{B}}^{-1}$ . The large difference in magnitude is explained reasonably well by taking into account the transferred fields from neighbouring atoms. In the first approximation, the hyperfine coupling constant is decomposed into an intra-atomic (on-site) field and a transferred field from nearest-neighbour atoms. Assuming that the transferred field is proportional to the vector sum of nearest-neighbour magnetic moments, the relations  $|A_{\text{P}}| = |A_{\text{on}} + 6A_{\text{tr}}| = 22.2 \text{ T } \mu_{\text{B}}^{-1}$  and  $|A_{\text{AF}}| = |A_{\text{on}} - 2A_{\text{tr}}| = 4.6 \text{ T } \mu_{\text{B}}^{-1}$  hold for the paramagnetic and magnetically ordered state, respectively, where  $A_{\text{on}}$  is the field produced by intra-atomic 3d electrons and  $A_{\text{tr}}$  the transferred field produced by each nearest-neighbour atom. This is based on the fact that four of the six nearest-neighbour magnetic moments cancel in the antiferromagnetic spin configuration. Solving these equations, we have  $|A_{\text{on}}| = 9.0 \text{ T } \mu_{\text{B}}^{-1}$  and  $|A_{\text{tr}}| = 2.2 \text{ T } \mu_{\text{B}}^{-1}$ , both of which are reasonable for metallic Mn compounds.

## 5. Concluding remarks

To consider the magnetic structure of  $\text{YMn}_2$ , we carried out both neutron diffraction and NMR experiments. It should be emphasized that local probes such as NMR give useful information

for determining the spin direction and enable us to discriminate between magnetic structures which are equivalent in the reciprocal space. The main experimental results and their analyses are summarized as follows:

- (i) The paramagnetic Knight shift shows an appreciable anisotropy, suggesting anisotropic local susceptibility. All of the NMR results for the ordered state also indicate a strong local magnetocrystalline anisotropy, suggesting non-negligible spin-orbit coupling.
- (ii) We found unexpectedly a large frequency variation of the spin-echo decay time  $T_2$  in the helimagnetic state; this was explained in terms of a phenomenological model taking into consideration the dynamic motion of electron spins in the locally anisotropic magnetic system. As a result, the inconsistency among the previous NMR results was completely removed.
- (iii) The  $T_2$ -corrected NMR spectrum for the helimagnetic state was consistently explained assuming an anisotropy in the local field and a homogeneous distribution of the spin direction.
- (iv) The substitution of a small amount of Tb for Y induces a spin reorientation from the propagation vector  $\vec{Q} = [\tau 0 1]$  ( $\tau = 0.018$ ) with spins rotating in the  $\{100\}$  plane to  $\vec{Q} = [\tau \tau 1]$  ( $\tau = 0.015$ ) with  $\{111\}$ -plane rotation, but leaves the tetragonal lattice distortion as it is.

We recognized the magnetic ordering of  $\text{YMn}_2$  as the partial release of the geometrical frustration of the nearest-neighbour antiferromagnetic interaction in the corner-sharing tetrahedral lattice, and treated the ordered state as weakly coupled one-dimensional antiferromagnetic spin chains. In the ordered state with the tetragonal lattice symmetry, the frustration still remains, resulting in degeneracy of the spin direction. Therefore secondary and minor interactions should determine the actual structure. We suggested here that the magnetocrystalline anisotropy, probably via the spin-orbit coupling, plays an important role in selecting the spin direction and discussed the possibility of double-axial helimagnetic structures. In particular, the tetragonal lattice symmetry below  $T_N$  is rather naturally understood if we assume a double-axial state, which may be classified as a kind of ordered state of 'orbitals' in a very broad sense. The spin reorientation induced by the Tb substitution was interpreted as a symmetry lowering from a coherent proper screw state with high magnetic symmetry to an asymmetric but locally preferable configuration in the easy-plane anisotropy perpendicular to the local symmetry axis. The long-period moderation was ascribed to the lattice distortion induced to release the frustration.

The strong frequency dependence of  $T_2$  found in the present study indicates that the  $T_2$ -correction of the NMR spectrum is crucially important in discussing the magnetic structure not only for  $\text{YMn}_2$  but also for general anisotropic magnetic systems.

### Acknowledgments

The authors are indebted to Y Shimojo at JAERI for assistance in neutron diffraction experiments, M Mekata at Fukui University, K Yoshimura and H Wada for helpful discussion and S Giri and T Yamasaki for help with the susceptibility measurements. They are also grateful to R Iehara for technical support at Kyoto University. One of the authors (HN) thanks the staff at JAERI for kind hospitality during a stay there. This work was partially supported by a Grant-in-Aid for Scientific Research given by the Ministry of Education, Science, Sports and Culture of Japan.

## References

- [1] For example, Rossat-Mignod J 1987 *Methods of Experimental Physics* vol 2, part C (Orlando, FL: Academic) p 69
- [2] As an example, see Nakamura H, Kitaoka Y, Asayama K, Ōnuki Y and Shiga M 1994 *J. Phys.: Condens. Matter* **6** 10 567
- [3] Ballou R, Deportes J, Lemaire R, Nakamura Y and Ouladdiaf B 1987 *J. Magn. Magn. Mater.* **70** 129
- [4] Cywinski R, Kilcoyne S H and Scott C A 1991 *J. Phys.: Condens. Matter* **3** 6473
- [5] Vokhnyanin A P, Menshikov A Z and Pirogov A N 1994 *Fiz. Tverd. Tela* **36** 340 (Engl. Transl. 1994 *Sov. Phys.—Solid State* **36** 186)
- [6] Nakamura Y, Shiga M and Kawano S 1983 *Physica B* **120** 212
- [7] Terao K 1996 *J. Phys. Soc. Japan* **65** 1413
- [8] Ballou R, Deportes J, Lemaire R, Ouladdiaf B and Rouault P 1988 *Proc. 4th Int. Conf. on Physics of Magnetic Materials* ed W Gorzkowski, H K Lachowicz and H Szymczak (Singapore: World Scientific) p 427
- [9] Tagawa Y, Sakurai J, Komura Y, Wada H, Shiga M and Nakamura Y 1985 *J. Phys. Soc. Japan* **54** 591
- [10] Gaidukova I Yu and Markosyan A S 1982 *Phys. Met. Metalloved.* **54** 168
- [11] Gaidukova I Yu, Kelarev V V, Markosyan A S, Menshikov A Z and Pirogov A N 1988 *J. Magn. Magn. Mater.* **72** 357
- [12] Yoshimura K and Nakamura Y 1983 *J. Magn. Magn. Mater.* **40** 55
- [13] Bertier Y, Deportes J, Horvatic M and Rouault P 1988 *J. Physique Coll.* **49** C8 261
- [14] Kapusta Cz, Przewoznik J, Zukrowski J, Spiridis N, Figiel H and Krop K 1990 *Hyperfine Interact.* **59** 353
- [15] Figiel H, Kapusta Cz, Spiridis N, Riedi P C and Lord J S 1993 *Z. Phys. Chem.* **179** 467
- [16] Nakamura H, Shiga M and Metoki N 1996 *J. Magn. Magn. Mater.* **163** L1
- [17] Nakamura H, Takayanagi F and Shiga M 1998 *J. Magn. Magn. Mater.* **177–181** 595
- [18] Shiga M, Nakamura H and Metoki N 1999 *J. Magn. Magn. Mater.* **196+197** 751
- [19] Shiga M 1988 *Physica B* **149** 293
- [20] Giri S, Nakamura H and Shiga M 2000 *Phys. Rev. B* **61** 12 233
- [21] Zheng G-q, Nishikido K, Ohnishi K, Kitaoka Y, Asayama K and Hauser R 1999 *Phys. Rev. B* **59** 13 973
- [22] McHenry M R, Silbernagel B G and Wernick J H 1972 *Phys. Rev. B* **5** 2958
- [23] Narath A 1967 *Phys. Rev.* **162** 162
- [24] Moriya T 1956 *Prog. Theor. Phys.* **16** 23  
Moriya T 1956 *Prog. Theor. Phys.* **16** 641
- [25] Ruderman M A and Kittel C 1954 *Phys. Rev.* **96** 99
- [26] Suhl H 1959 *J. Physique Radium* **20** 333
- [27] Nakamura T 1958 *Prog. Theor. Phys.* **20** 542
- [28] Sherrington D 1958 *J. Appl. Phys.* **39** 502
- [29] Abelyashev G N, Berzhansky V N, Fedotov Yu V, Polulyakh S N and Sergeev N A 1998 *J. Magn. Magn. Mater.* **184** 222 and references therein
- [30] Terao K 1997 *J. Phys. Soc. Japan* **66** 1796
- [31] Giebultowicz T M, Samarth N, Luo H, Furdyna J K, Klosowski P and Rhyne J J 1992 *Phys. Rev. B* **46** 12 076
- [32] Ritter C, Cywinski R and Kilcoyne S H 1997 *Physica B* **234–236** 596
- [33] Nakamura H and Shiga M 2001 *Proc. Int. Conf. on Magnetic Materials (Calcutta, 2000); J. Alloys Compounds* at press
- [34] Nakamura H *et al* unpublished